

Research Article

Investigation into the Mechanism of the Steel Particle Feeding Process: A Numerical and Experimental Study

Lei Li ¹, Xueyang Xing ², Fangxiang Wang ³, and Xiaodong Dai ¹

¹College of Petroleum Engineering, Shengli College China University of Petroleum, Dongying 257061, China

²Department of Architectural Engineering, Binzhou University, Binzhou 256600, China

³Bohai Drilling Downhole Technology Service Company, Tianjin 300270, China

Correspondence should be addressed to Xueyang Xing; xingxuey666@126.com

Received 5 November 2020; Revised 28 December 2020; Accepted 7 January 2021; Published 22 January 2021

Academic Editor: Shiyuan Zhan

Copyright © 2021 Lei Li et al. This is an open access article distributed under the Creative Commons Attribution License, which permits unrestricted use, distribution, and reproduction in any medium, provided the original work is properly cited.

The particle feeding system is a prerequisite for the realization of particle impact drilling technology. Because of the high density, the storage and flow of the steel particle are different from those of the other nonviscous particles. The differential equation of the particle movement was built with the liquid bridge force model and the discrete element method. The dynamic movement process and the distribution state of particles in the high-pressure tank were analyzed. For 1 mm steel particles, the mass flow rate decreased with the increase in water content. For 2 mm and 3 mm steel particles, the water content of 15% and 20% was the dividing point of the mass flow rate from increasing to decreasing. When the water content was 10% and 20%, the mass flow rate increased with the steel particle size. But when the water content was 30% and 40%, the mass flow rate decreased with the steel particle size. The study of the control mechanism of the uniformity and stability of particles showed that the funnel flow was the major reason causing the instability and blocking of the feeding process. This research results can provide a basis for the further improvement of the differential pressure feeding system.

1. Introduction

Due to the poor drillability of the hard formation and the strong abrasive formation for the unconventional oil and gas reservoir, many problems are met during the drilling operation of the unconventional oil and gas reservoir, such as the low ROP and the complex downhole problems. The rock breaking efficiency of the steel particles with large velocity and high frequency is satisfactory, so the particle impact drilling technology can significantly improve the mechanical drilling speed of the hard formation and the highly abrasive formation. Therefore, the particle impact drilling technology is a good choice for exploration and development of unconventional reservoirs [1]. The particle feeding system is a guarantee of the particle impact drilling technology [2]. How to feed particles from the high-pressure drilling fluid to the mixer continuously and stably is an interesting research topic [3].

The wet particle system is a multiphase structure composed of the dense solid particles and the interstitial fluid [4]. The liquid bridge forms between contacting particles, and it results in viscous force. The increase in viscosity has a negative effect on the flow of the particles in the high-pressure tank [5]. But on the other hand, this strong combination effect is beneficial to the other processes [6]. The gas-solid flow in a pseudo 2D fluidized bed of wet particles with the presence of immersed tubes was studied. The gas-solid flow characteristics around the immersed tubes and the effects of immersed tubes, adhesive force, and fluidization velocity on the fluidization of wet particles were analyzed. The various models and experimental results for liquids at small and moderate viscosities were summarized. Several discrepancies between experiments at small liquid viscosities and models were found, and reasons for these differences were discussed. A fast and accurate framework for simulating spheroids in periodic Stokes flow was built, which was based

on the completed double-layer boundary integral formulation [7–10]. In view of the particle impact drilling technology, the steel particles in the high-pressure tank contain a certain amount of water, and it often leads to the phenomenon of particle blocking and arching. High density is a typical feature of the steel particle, but there is no similar research about the particle with high density. The problems of discontinuity, instability, and arching often appear in the particle hydraulic feeding system, and it is due to the lack of research on the particle motion law in the high-pressure tank. Consequently, the reasons for the instability and blockage of particle feeding should be studied.

In order to analyze the behavior of the wet particles, it is necessary to determine the geometric properties and the physicochemical properties of the particle and the liquid phase [11–14]. Based on the flow of the wet particles in the high-pressure tank, the motion of the wet particles can be described and the behavior characteristics of the wet particle system can be studied. This research was aimed at researching the particle feeding mode under differential pressure [15–17]. The liquid bridge force model and the discrete particle method were combined to simulate the particle motion [18–20]. The dynamic change process and the particle distribution state of particle motion in the high-pressure tank were analyzed. The internal mechanism of particle feeding instability and blockage was clarified. This research can promote the popularization and application of differential pressure feeding.

2. Methodology

2.1. Computational Model

2.1.1. Mechanical Analysis. Based on the feeding mode under differential pressure, the movement rule of the particles in the high-pressure tank was studied. The high-pressure fluid entered from the inlet, and a part of the fluid entered the high-pressure tank through the pressure balance pipeline (Figure 1). This ensured the pressure in the high-pressure tank consistent with the inlet pressure, and it played a role in preboosting.

2.1.2. Physical Model. The focus of this research was the movement and the feeding law of particles in the high-pressure tank, and the aim was to study the flow instability and the particle blockage reasons. The physical model of the high-pressure tank was established (Figure 2). The calculation model parameters, high-pressure tank parameters, and particle parameters required in the study are shown in Table 1.

The soft sphere model of the DEM method was used to study the movement of particles in the high-pressure tank [21–23]. The model of indirect contact force between particles was represented by the spring damper friction device. The resultant forces were composed of the elastic force, the viscous damping force, and the friction force. The relative displacement between particles determined the magnitude of the elastic force. The normal elastic force was determined by the Hertz contact theory model. The tangential elastic

force was determined by the Mindlin and Deresiewicz theory [24, 25]. The normal force $\vec{f}_{cn,ij}$ and the tangential force $\vec{f}_{ct,ij}$ were, respectively, described as the following formula.

$$\begin{aligned}\vec{f}_{cn,ij} &= \left[\frac{4}{3} E^* (R^*)^{0.5} \delta_{n,ij}^{1.5} \right] \vec{n}, \\ \vec{f}_{ct,ij} &= \mu \left| \vec{f}_{cn,ij} \right| \left[1 - \left(1 - \frac{|\delta_{t,ij}|}{\delta_{\max}} \right)^{1.5} \right] \vec{t},\end{aligned}\quad (1)$$

where E^* is the relative elastic model of two particles (MPa). When the elastic modulus of both particles is E , $E^* = E/2(1 - \nu^2)$. ν is Poisson's ratio of the particle. R^* is the relative radius of two particles (m). $R^* = R_i R_j / (R_i + R_j)$, where R_i and R_j are the radius of particle i and particle j , respectively. μ is the particle friction coefficient. $\delta_{n,ij}$ is the normal displacement (m). $\delta_{t,ij}$ is the tangential displacement (m). δ_{\max} is the maximum tangential displacement without sliding (m). $\delta_{\max} = \delta_{n,ij} \mu ((2 - \nu)/2(1 - \nu))$.

The normal component $\vec{f}_{dn,ij}$ and the tangential component $\vec{f}_{dt,ij}$ of the viscous damping force were described by the following formula, respectively.

$$\begin{aligned}\vec{f}_{dn,ij} &= c_n (\vec{V}_{ij} \cdot \vec{n}) \vec{n}, \\ \vec{f}_{dt,ij} &= c_t (\vec{V}_{ij} \times \vec{n}) \times \vec{n},\end{aligned}\quad (2)$$

where c_n is the normal viscous damping coefficient. c_t is the tangential viscous damping coefficient. V_{ij} is the relative velocity at the contact of particle i and particle j (m/s).

When multiple particles contacted with each other, the contact force and moment of particles were $\sum \vec{F}_c$ and $\sum \vec{M}$.

$$\begin{aligned}\sum \vec{F}_c &= \sum_{i=1}^n \left(\vec{f}_{cn,ij} + \vec{f}_{dn,ij} + \vec{f}_{ct,ij} + \vec{f}_{dt,ij} \right), \\ \sum \vec{M} &= \sum_{i=1}^n \left(\vec{R}_i \times \vec{F}_{t,ij} \right).\end{aligned}\quad (3)$$

Because there was a certain amount of fluid between particles, it was easy to form the liquid bridge and generate the liquid bridge force. The liquid bridge force F_l included the static capillary force f_{cap} and the dynamic viscous force f_v . The static capillary force was calculated by Fisher's method [26].

$$\begin{aligned}f_{\text{cap}} &= \pi \rho_2^2 \Delta p_0 + 2\pi \rho_2 \sigma_s = \pi \rho_2 \sigma_s \left(1 + \frac{\rho_2}{\rho_1} \right), \\ \rho_1 &= \frac{[R_0(1 - \cos \phi) + h/2]}{\cos(\phi + \theta)}, \\ \rho_2 &= R_0 \sin \phi - [1 - \sin(\phi + \theta)] \rho_1,\end{aligned}\quad (4)$$

where θ is the contact angle (rad). ϕ is the half filling angle

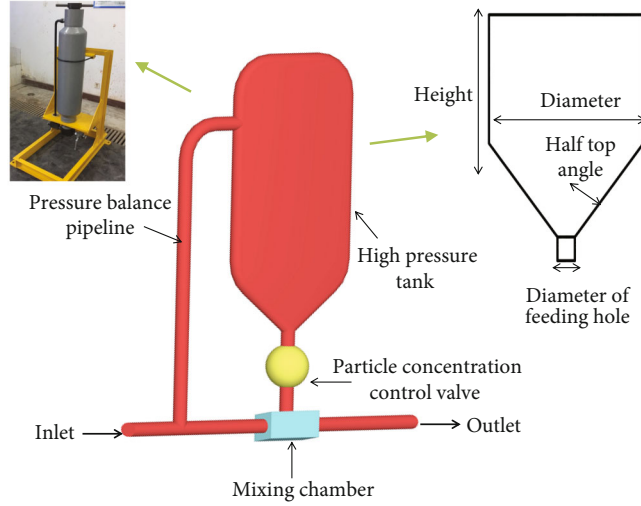


FIGURE 1: The working principle of the differential pressure feeding system.

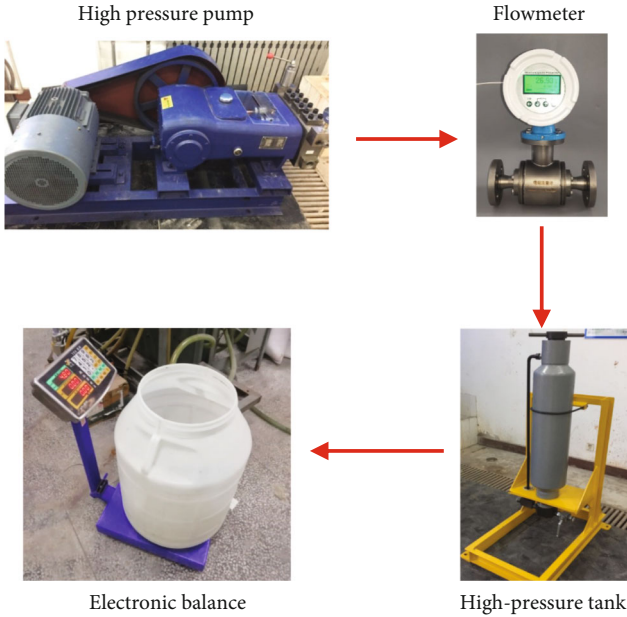


FIGURE 2: The experimental equipment and the procedure.

(rad). σ_s is the fluid surface tension (N/m). Δp_0 is the capillary pressure (Pa). ρ_1 is the radius of the liquid bridge (m). ρ_2 is the neck radius of the liquid bridge (m). R_0 is the particle radius (m). h is the particle spacing (m).

The dynamic viscous force was analyzed by Washino et al. [27]. The normal component and tangential component of the viscous force of the liquid bridge were, respectively, described by the following formulas.

$$f_{vn} = 6\pi\eta V_n \frac{R_0^2}{4h}, \quad (5)$$

$$f_{vt} = \left(\frac{24}{15} \ln \frac{R_0}{2h} + 2.8764 \right) \pi\eta R_0 V_t, \quad (6)$$

where V_n is the normal relative velocity (m/s). V_t is the tangential relative velocity (m/s). η is the viscosity coefficient of fluid (Pa·s).

2.1.3. *Motion Equation and Solution.* The particle i was affected by the ejecting force F_g , the contact force $\sum F_c$ of surrounding particles to particle i , the liquid bridge force F_l between particles, and the resultant moment $\sum M$. All the resultant forces and the moments of the particles could be described by Newton's second law at any time.

$$\begin{aligned} \frac{\partial^2 x_i(t)}{\partial t^2} &= \frac{\sum F_i}{m_i}, \\ \frac{\partial^2 \theta_i(t)}{\partial t^2} &= \frac{\sum M_i}{I_i}, \end{aligned} \quad (7)$$

where $i = 1, 2, 3 \dots, n$. x_i is the translational displacement (m). θ_i is the angular displacement (rad). m_i is the particle mass (kg). I_i is the moment of inertia (kg·m²).

The acceleration at time t was discretized by the central difference scheme, and the displacement at time t could be obtained.

$$\begin{aligned} x_i^{(t+\Delta t)} &= x_i^{(t)} + \frac{\partial x_i^{(t+(\Delta t/2))}}{\partial t} \Delta t, \\ \theta_i^{(t+\Delta t)} &= \theta_i^{(t)} + \frac{\partial \theta_i^{(t+(\Delta t/2))}}{\partial t} \Delta t. \end{aligned} \quad (8)$$

During the process of solving the particle motion equation, the calculation of force and displacement was carried out in the same time step. The displacement of time $t + \Delta t$ was derived from the acceleration of time t in the form of central difference. The particle surface bore new contact force and moment at the new position. The resultant force and the resultant moment of particle i were calculated, and the results were returned to formulas (5) and (6) for cyclic iteration. The

TABLE 1: Calculation parameters.

Items	Parameters	Units	Value
Steel particles	Diameter	m	0.0008-0.003
	Density	kg/m ³	7400
	Elastic modulus	Pa	2700000
	Poisson's ratio		0.3
	Diameter	mm	200
High-pressure tank	Diameter of the feeding hole	mm	25
	Height	mm	400
	Half of apex angle	°	45°
	Pressure	MPa	20
Operation	Diameter of the orifice	mm	9.5
	Friction coefficient between particles and tank wall		0.3
Calculation	Friction coefficient between particles		0.3
	Surface tension	N/m	0.06
Fluid	Viscosity	Pa·s	0.002

motion form of each particle in the particle aggregate was obtained until the end of the required calculation process.

2.2. Indoor Experiment. Based on the above analysis on the dynamic change process of the particles, the particle tank was machined, and the particle feeding experiment system was established. The accuracy of numerical simulation results was verified by the indoor experiment.

The experimental equipment mainly included a high-pressure water supply system, a particle feeding experimental system, and an electronic balance (Figure 2). The mass flow rate of steel particles represented the feeding rate of particles in this research. The steel particle mass flow rate was defined as the mass of steel particles flowing out of the high-pressure tank in unit time.

Take 10 s as the unit time, and weight the total weight of particles and water after the bucket was connected. Remove the water and dry the particles, and weigh the particles. Then, convert it into the steel particle mass flow rate.

3. Results and Discussions

There were two main flow patterns of the steel particles in the high-pressure tank during the feeding process [28–31]. One was the overall flow, and all the steel particles flowed at the same time during the feeding. It could be described as the “first in-first out” flow pattern, and there was relative movement between the steel particles and the wall. The other was the funnel flow, the center flow was faster, and the boundary flow was slower. The flow area was funnel-shaped during the feeding. In addition to the flow region, there was a “dead zone” in which the steel particles were stationary. Most of the steel particles on the top of the high-pressure tank flowed out of the high-pressure tank before the steel particles near the edge.

The reason for the funnel flow was that the upper steel particles flowed from the inner surface to the active area in the middle, where they moved downward and flowed out of

the high-pressure tank. As the particles flowed down the tube channel at the upper end of the feeding hole, the upper surface of the particles fell. The upper particles continuously flowed into the tube channel and flowed out of the tank; then, the “advanced backward” flow effect formed. For funnel flow, there was an extreme case that only the vertical center area has flow which is called plug flow.

When the bottom of the high-pressure tank opened, the discharge mass flow rate began to increase with time. After a certain period of time, the mass flow rate began to fluctuate, but it basically changed around a constant value. The reason for the pulsation was the formation of dynamic arch during the process of steel particle flow. The arch was unstable, and it resulted in density wave during unloading. The magnitude of the pulsation depended on the contact force in the shear direction.

The whole unloading process was divided into two stages, the initial acceleration stage and the flow stability stage until the end of unloading. When the bottom of the high-pressure tank was just opened, the force supporting the column disappeared, and the particles near the feeding hole fell freely. Then, the movement of other steel particles in the tank changed. The initial acceleration period was very short, and most of the unloading process was in stable flow.

The discharge mass flow rate was an important index to study the influence of the geometric parameters and the steel particle characteristic parameters. Compared with the funnel flow, the mass flow rate of the whole flow was larger and the fluctuation of the flow rate was smaller. Consequently, its flow was relatively stable.

3.1. Analysis of the Particle Motion Process. Figure 3 describes the flow state and the vertical velocity distribution of particles in the high-pressure tank at different times. In order to track the movement and the position of particles in the high-pressure tank, the tracer layer particles (blue particles) were set at four different heights. In the velocity distribution diagram of particles, the length of arrow represented the size

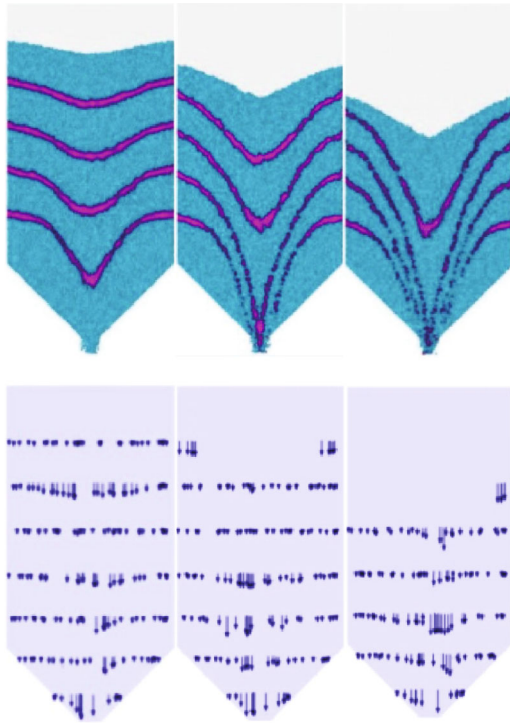


FIGURE 3: Flow state and vertical velocity distribution of steel particles when the half of apex angle was 45° at different times. The upper part was the flow state of steel particles, and the lower part was the vertical velocity distribution of steel particles. (a) Time was 10 s. (b) Time was 25 s. (c) Time was 40 s.

of velocity, and the density of arrow represented the number of particles participating in the flow. In the process of the particle feeding, the particles in the middle part of the tank flowed faster than the particles near the tank wall. The tracer layer showed a parabola shape.

The flow in the middle of the high-pressure tank was the vertical flow (Figure 3). The particles in the upper area on both sides of the vertical flow area were easy to enter the hopper under the sliding action, and it could be described as the fast flow area. Below the fast flow area, the particle flow area near the tank wall was the slow flow area. However, due to the friction between the particles and the viscous force of the liquid bridge, the velocity of the particles near the tank wall in the lower part of the slow flow region was almost zero, which could be described as the stagnation area. During the process of funnel flow particle feeding, the tangential friction caused by the relative motion of the particles increased. The friction between the particles and the viscous force of the liquid bridge caused the dissipation of injected kinetic energy of the particles, and this hindered the flow of particles.

3.2. Effect of the Water Content on the Mass Flow Rate. The water content of the wet steel particles in the high-pressure tank directly affected the liquid bridge force between the steel particles and the flow characteristics of the steel particles. The mass fraction of 1 mm steel particles with different water contents was calculated (Figure 4). For 1 mm steel particles, the effect of the liquid bridge force became more obvious with the increase in the water content. When the moisture

content was 30%, the mass flow rate of the steel particles decreased significantly. For example, the steel particle mass flow rate reduced from 39.2% to 15.8% when the unloading was in half. When the moisture content increased to 40%, the steel particles were agglomerated at the beginning of the feeding hole, and the unloading mass fraction remained at 11.2%. Therefore, the mass flow rate of steel particles decreased with the increase in water content (Figure 5).

For steel particles with relatively small particle size (0.8 mm, 1.2 mm, and 1.4 mm), the above rules were also applicable. However, for steel particles with relatively large particle size (2 mm, 3 mm), the influence of water content on the mass flow rate was different. When the water content increased from 5% to 15%, the mass flow rate of steel particles increased. As the moisture content continued to increase, the mass flow rate of steel particles began to decrease. When the water content increased to 15%, the decrease was very obvious. In order to prove the correctness of the simulation results, the effect of the water content of 2 mm and 3 mm steel particles on the mass flow rate was tested. The experimental results were compared with the simulation results (Figure 5).

The results showed that the simulation results were in good agreement with the experimental results. The water content of 15% and 20% was the dividing point of the mass flow rate from increasing to decreasing. For 2 mm and 3 mm steel particles, the amount of water needed to build the liquid bridge was relatively large. When the water content was less than 15% and 20%, it was not enough to build a liquid bridge. The water infiltrated the surface of the steel particles. On the contrary, it played a certain role in lubricating the flow of the steel particles, so the mass flow rate increased. With the further increase in water content, the liquid bridges formed between the steel particles, and the viscous force between the steel particles increased. The kinetic energy of the steel particles dissipated, and the movement of steel particles was hindered. So the mass flow rate decreased. For 2 mm steel particles, the inflection point of water content was 15%. For larger steel particles, the inflection point should be different from that for 2 mm steel particles. With the increase in water content, the mass flow rate of steel particles must not have a single downward trend. There must be a process of rising first and then falling, and this was related to the amount of water required for the completion of the bridge.

3.3. Effect of the Steel Particle Size on the Mass Flow Rate.

When the water content was 10% and 20%, the mass flow rate of the steel particles increased with the increase in steel particle size, and the relationship between particle size and mass flow rate was approximately linear (Figure 6). When the water content was 30% and 40%, the mass flow rate of the steel particles decreased with the increase in steel particle size. This was mainly because the liquid bridge force hindered the flow of steel particles.

The smaller the particle size was, the more obvious the influence of liquid bridge force was. For 1 mm steel particles, the ratio of liquid bridge force to mass force changed with the steel particle spacing. The ratio was between 0.36 and 1.06. The liquid bridge force and mass force were of the same order of magnitude. The effect of liquid bridge force was

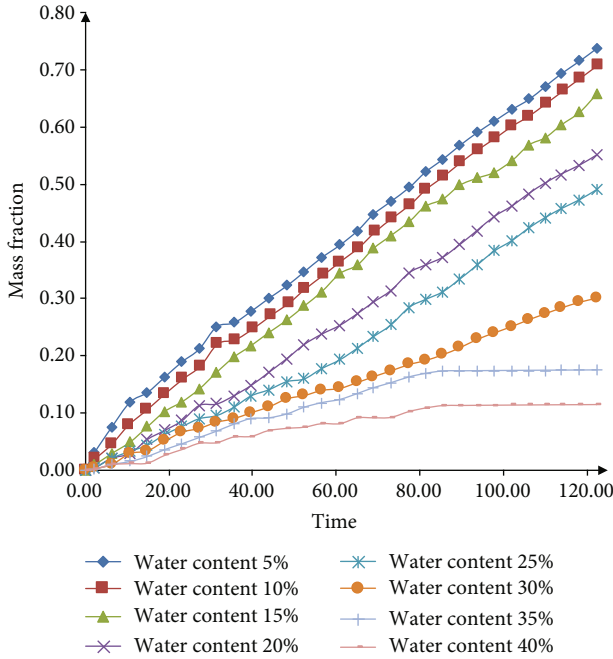


FIGURE 4: The mass fraction of 1 mm steel particles with different water contents.

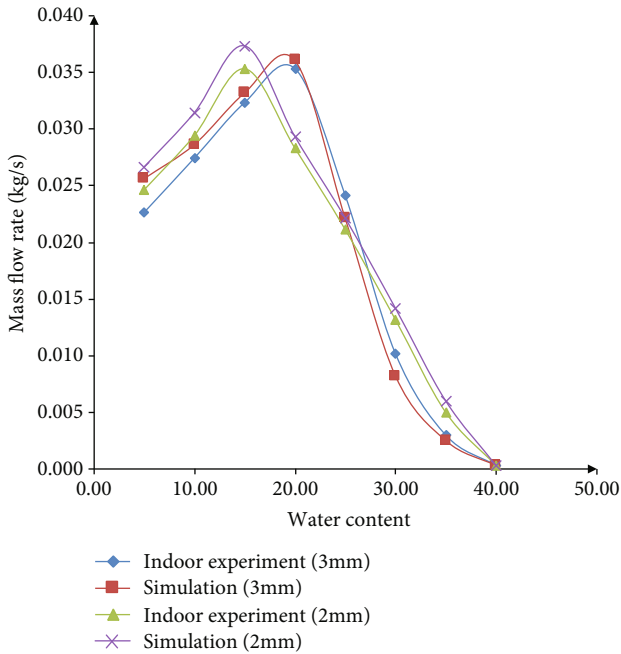


FIGURE 5: Comparison of simulation results and experimental results of 2 mm and 5 mm particles with different water contents.

significant. For 2 mm steel particles, the ratio of mass force to liquid bridge force was between 0.01 and 0.042, and the effect of the liquid bridge force on the flow of the steel particles was obviously less than that of 1 mm steel particles. The energy dissipation caused by the liquid bridge force hindered the movement of the steel particles and slowed down the movement.

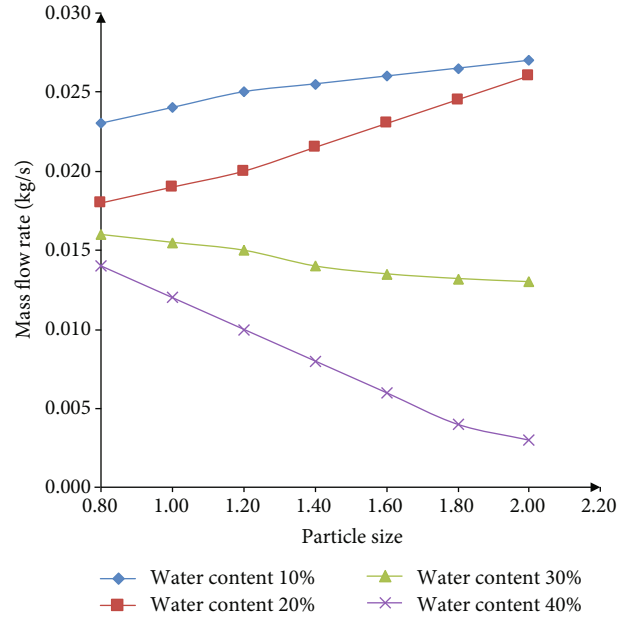


FIGURE 6: Comparison of the mass flow rate with the different particle sizes.

3.4. Internal Mechanism of Particle Blockage. The results of the numerical simulation showed that three kinds of effect resulted in the blockage of the feeding hole and the instability of the feeding process, including the viscous effect of the liquid bridge force, the arching effect of the asymmetric flow, and the collapse of the particle aggregate.

- (1) The viscous action of the bridge force: the centrifugal pump was used to transport the fluid, and the pressure balance pipeline sent the fluid to the high-pressure tank, so the particles in the high-pressure tank were surrounded by the fluid. Due to the funnel flow, the particles in the high-pressure tank had a slow flow area and a stagnant area. The liquid bridge was easy to form between the particles, and the viscous force between the particles increased. Many particles were connected with each other to form bridges, and the particles aggregated into a group (Figure 7)
- (2) The arching effect of the asymmetric flow: the particle velocity distribution showed that the flow of the particles in the high-pressure tank was asymmetric under the effect of pressure difference and gravity. Sometimes the flow was fast on the left side, and sometimes the flow was fast on the right side. In the alternating moment of left and right flow, the flow was symmetrical and presented the form of converging flow. The particles rushed to the middle of the feeding hole, and the feeding speed of particles was fastest. It was easy to form an unstable dynamic arch. During the process of forming and destroying the dynamic arch, the feeding hole produced the particle flow density wave which caused the instability of

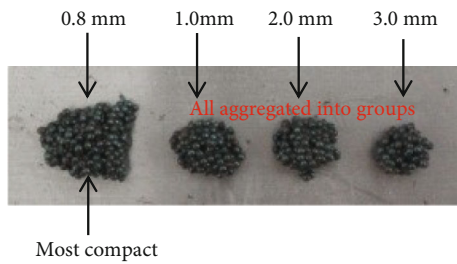


FIGURE 7: Particle aggregate with different sizes.

particle feeding. Because the feeding speed of particles was too fast, it was easy to cause particles to squeeze each other to achieve a force balance and form a mechanical arch. Thus, a blocking phenomenon would occur

- (3) The collapse of particle aggregate: during the process of particle feeding, the middle part of the high-pressure tank presented a flow state similar to that of the funnel. When the cone of the funnel was steep, the particles in the rapid flow area slid into the funnel with a large speed. It had a compaction effect on the particles in the lower part, or even the whole particle aggregate collapsed. Then, a large number of particles in the feeding hole turned compact, and this would result in the blocking accident of the feeding hole

4. Conclusion

In this research, the liquid bridge force model and the discrete particle method were combined to simulate the particle motion. The dynamic change process and the particle distribution state of particle motion in the high-pressure tank were analyzed. This research can provide bases for the design of the particle feeding system.

- (1) The numerical simulation results and the indoor experiment showed that the water content and the size of steel particles affect the mass flow rate. With the increase in water content, the mass flow rate of steel particles must not have a single downward trend. The smaller the particle size was, the more obvious the influence of liquid bridge force on the flow of steel particles was
- (2) There are three kinds of effect that resulted in the blockage of the feeding hole and the instability of particle feeding, including the viscous effect of the liquid bridge force, the arching effect of the asymmetric flow, and the collapse of the particle aggregate
- (3) The future research will focus on the structure design of the feeding tank, and the effect of different transport methods on the uniformity of particle injection should be investigated

Data Availability

The data used to support the findings of this study are available from the corresponding author upon request.

Conflicts of Interest

The authors declare that they have no conflicts of interest.

Acknowledgments

The work was supported by the National Natural Science Foundation of China (51808041), the Dongying Science Development Fund (DJ2020008), the Youth Innovation Team Science and Technology Development Program of Shandong Province Higher Educational Institutions (2019KJA024), the construction team of Shandong Province University Youth Creative Talents Introduction and Education Plan: research and innovation team of complex oil and gas well drilling engineering, Project of Natural Science Foundation of Shandong Province (ZR2019PEE005), and the Binzhou University Doctoral Research Start-up Fund Project (2017Y20).

References

- [1] F. X. Wang, R. H. Wang, W. D. Zhou, and G. Chen, "Numerical simulation and experimental verification of the rock damage field under particle water jet impacting," *Journal of Petroleum Science and Engineering*, vol. 102, pp. 169–179, 2017.
- [2] J. Zhao, G. Zhang, Y. Xu et al., "Mechanism and effect of jet parameters on particle waterjet rock breaking," *Powder Technology*, vol. 313, pp. 231–244, 2017.
- [3] J. Zhao, G. Zhang, Y. Xu, R. Wang, W. Zhou, and D. Yang, "Experimental and theoretical evaluation of solid particle erosion in an internal flow passage within a drilling bit," *Journal of Petroleum Science and Engineering*, vol. 160, pp. 582–596, 2018.
- [4] A. Soames, S. Al-Ansari, S. Iglauer, A. Barifcani, and R. Gubner, "Effect of wettability on particle settlement behavior within mono-ethylene glycol regeneration pre-treatment systems," *Journal of Petroleum Science and Engineering*, vol. 179, pp. 831–840, 2019.
- [5] K. Washino, E. L. Chan, T. Matsumoto, S. Hashino, T. Tsuji, and T. Tanaka, "Normal viscous force of pendular liquid bridge between two relatively moving particles," *Journal of Colloid and Interface Science*, vol. 494, pp. 255–265, 2017.
- [6] S. Brulin, C. Tropea, and I. V. Roisman, "Pinch-off of a viscous liquid bridge stretched with high Reynolds numbers," *Colloids and Surfaces A: Physicochemical and Engineering Aspects*, vol. 587, article 124271, 2020.
- [7] M. Zhao, D. Liu, J. Ma, and X. Chen, "CFD-DEM simulation of gas-solid flow of wet particles in a fluidized bed with immersed tubes," *Chemical Engineering and Processing - Process Intensification*, vol. 156, article 108098, 2020.
- [8] L. af Klinteberg and A.-K. Tornberg, "A fast integral equation method for solid particles in viscous flow using quadrature by expansion," *Journal of Computational Physics*, vol. 326, pp. 420–445, 2016.
- [9] P. Ding, S. Bakalis, and Z. Zhang, "Foamability in high viscous non-Newtonian aqueous two-phase systems composed of surfactant and polymer," *Colloids and Surfaces A: Physicochemical and Engineering Aspects*, vol. 582, article 123817, 2019.
- [10] M. Liang, X. Xin, W. Fan, H. Sun, Y. Yao, and B. Xing, "Viscous properties, storage stability and their relationships with microstructure of tire scrap rubber modified asphalt," *Construction and Building Materials*, vol. 74, pp. 124–131, 2015.

- [11] L. Zhang and C. Y. Wu, "Discrete element analysis of normal elastic impact of wet particles," *Powder Technology*, vol. 362, pp. 628–634, 2020.
- [12] J. Shabaniyan, M. A. Duchesne, A. Runstedtler, M. Syamlal, and R. W. Hughes, "Improved analytical energy balance model for evaluating agglomeration from a binary collision of identical wet particles," *Chemical Engineering Science*, vol. 223, article 115738, 2020.
- [13] B. Buck and S. Heinrich, "Collision dynamics of wet particles: comparison of literature models to new experiments," *Advanced Powder Technology*, vol. 30, no. 12, pp. 3241–3252, 2019.
- [14] H. Wang, A. S. Verdugo, J. Sun, J. Wang, Y. Yang, and F. H. Jiménez, "Experimental study of bubble dynamics and flow transition recognition in a fluidized bed with wet particles," *Chemical Engineering Science*, vol. 211, article 115257, 2020.
- [15] Z. Sun, L. Liang, Q. Liu, and X. Yu, "Effect of the particle injection position on the performance of a cyclonic gas solids classifier," *Advanced Powder Technology*, vol. 31, no. 1, pp. 227–233, 2020.
- [16] S. V. Karthic, M. S. Kumar, G. Nataraj, and P. Pradeep, "An assessment on injection pressure and timing to reduce emissions on diesel engine powered by renewable fuel," *Journal of Cleaner Production*, vol. 255, article 120186, 2020.
- [17] S. Wang, V. Karthickeyan, E. Sivakumar, and M. Lakshmikandan, "Experimental investigation on pumpkin seed oil methyl ester blend in diesel engine with various injection pressure, injection timing and compression ratio," *Fuel*, vol. 264, article 116868, 2020.
- [18] Y. Tsunazawa, D. Fujihashi, S. Fukui, M. Sakai, and C. Tokoro, "Contact force model including the liquid-bridge force for wet-particle simulation using the discrete element method," *Advanced Powder Technology*, vol. 27, no. 2, pp. 652–660, 2016.
- [19] X. Sun and M. Sakai, "A liquid bridge model for spherical particles applicable to asymmetric configurations," *Chemical Engineering Science*, vol. 182, pp. 28–43, 2018.
- [20] Y. Chen, G. Jin, P. Zhang, S. A. Galindo-Torres, A. Scheuermann, and L. Li, "An efficient framework for particle-fluid interaction using discrete element lattice Boltzmann method: coupling scheme and periodic boundary condition," *Computers & Fluids*, vol. 208, article 104613, 2020.
- [21] L. M. Yao, Z. M. Xiao, J. B. Liu, Q. Zhang, and M. Wang, "An optimized CFD-DEM method for fluid-particle coupling dynamics analysis," *International Journal of Mechanical Sciences*, vol. 174, article 105503, 2020.
- [22] S. Golshan, R. Sotudeh-Gharebagh, R. Zarghami, N. Mostoufi, B. Blais, and J. A. M. Kuipers, "Review and implementation of CFD-DEM applied to chemical process systems," *Chemical Engineering Science*, vol. 221, article 115646, 2020.
- [23] J. Wang, L. Wang, M. Jia, Z. He, and L. Bi, "Construction and optimization method of the open-pit mine DEM based on the oblique photogrammetry generated DSM," *Measurement*, vol. 152, article 107322, 2020.
- [24] M. Chamekh, M. A. Latrach, and Y. Renard, "Frictional self-contact problem of elastic rods," *Journal of King Saud University - Science*, vol. 32, no. 1, pp. 828–835, 2020.
- [25] M. Wan, S. E. Li, H. Yuan, and W.-H. Zhang, "Cutting force modelling in machining of fiber-reinforced polymer matrix composites (PMCs): a review," *Composites Part A: Applied Science and Manufacturing*, vol. 117, pp. 34–55, 2019.
- [26] L. Chen, E. Bonaccorso, T. Gambaryan-Roisman, V. Starov, N. Koursari, and Y. Zhao, "Static and dynamic wetting of soft substrates," *Current Opinion in Colloid & Interface Science*, vol. 36, pp. 46–57, 2018.
- [27] K. Washino, E. L. Chan, H. Midou, T. Tsuji, and T. Tanaka, "Tangential viscous force models for pendular liquid bridge of Newtonian fluid between moving particles," *Chemical Engineering Science*, vol. 174, pp. 365–373, 2017.
- [28] R. Sharma and G. Setia, "Mechanical dry particle coating on cohesive pharmaceutical powders for improving flowability - a review," *Powder Technology*, vol. 356, pp. 458–479, 2019.
- [29] D. Kumar, A. Shenoy, J. Deutsch, and C. M. Schroeder, "Automation and flow control for particle manipulation," *Current Opinion in Chemical Engineering*, vol. 29, pp. 1–8, 2020.
- [30] P. Shi and R. Rzehak, "Lift forces on solid spherical particles in wall-bounded flows," *Chemical Engineering Science*, vol. 211, article 115264, 2020.
- [31] P. Shi and R. Rzehak, "Lift forces on solid spherical particles in unbounded flows," *Chemical Engineering Science*, vol. 208, article 115145, 2019.